

This is the pre-peer reviewed, authors' version of the Nanoscale article, published in its final form at <http://dx.doi.org/10.1039/C8NR01395K>

# Plasmonics with two-dimensional semiconductors “beyond graphene”: from basic research to technological applications

Amit Agarwal<sup>a</sup>, Miriam S. Vitiello<sup>b</sup>, Leonardo Viti<sup>b</sup>, Anna Cupolillo<sup>c</sup>, and Antonio Politano<sup>d</sup>

In this minireview, we explore the main features and the prospect of plasmonics with two-dimensional semiconductors. Plasmonic modes in each class of van der Waals semiconductors have their own peculiarities, along with potential technological capabilities. Plasmons of transition-metal dichalcogenides share features typical of graphene, due to their honeycomb structure, but with damping processes dominated by intraband rather than interband transitions, unlike graphene. Spin-orbit coupling strongly affects the plasmonic spectrum of buckled honeycomb lattices (silicene and germanene), while the anisotropic lattice of phosphorene determines different propagation of plasmons along the armchair and zigzag direction. We also review existing applications of plasmonics with two-dimensional materials in the fields of thermoplasmonics, biosensing, and plasma-wave Terahertz detection. Finally, we consider the capabilities of van der Waals heterostructures for innovative low-loss plasmonic devices.

## 1 Introduction

After the groundbreaking impact of graphene<sup>1,2</sup>, the scientific community is actively exploring other two-dimensional (2D) semiconductors “beyond graphene” for their promising applications capabilities, often complementary to those of graphene.<sup>3</sup> Different classes of 2D semiconductors have emerged in recent years: transition-metal dichalcogenides<sup>4</sup>; black phosphorus<sup>5</sup>; silicene/germanene<sup>6</sup>; and IV-VI semiconductors.<sup>7</sup>

Many innovative applications, widely used in our daily lives, are based on the exploitation of collective properties of matter (ferromagnetism, superconductivity, the quantum Hall effect and plasmonic excitations). Therefore, the comprehension of collective electronic excitations is crucial in order to develop new disruptive technologies for health, telecommunications, energy etc. In particular, the novel field of plasmonics has recently emerged,

in consideration of the progress of nanotechnology and nanofabrication. Plasmonics deals with the generation, propagation and detection of plasmonic excitations, which are collective electronic excitations produced by an electromagnetic field.<sup>8</sup> The field confinement and enhancement resulting from the interaction between matter and radiation can be technologically used for devising plasmonic devices for diverse applications, ranging from optics, biology, nanoelectronics and nanophotonics. Herein, we review the peculiarities, the applications, the pitfalls and the grand challenges of plasmonics with 2D semiconductors.

## 2 Peculiarities of plasmons in the Flatland

Plasmon modes are collective charge density excitations (oscillations), typically occurring in charged electron gases in solids in the presence of Coulomb interactions.

In the basic ‘classical’ picture, the long-wavelength plasmon dispersion (for  $q \ll k_F$ , with  $q$  the momentum and  $k_F$  the Fermi wave-vector) can be obtained from a macroscopic hydrodynamic model. Equating the force (due to Coulomb interactions) on the deviation of the electron density at a given location to the rate change of the momentum of the density deviations, and by using the continuity equation, the plasmon dispersion  $\omega_{pl}(q)$  in the long-wavelength limit can be obtained to be<sup>9,10</sup>

$$\omega_{pl}(q) = \sqrt{\frac{n}{m^*} q^2 V_q}, \quad (1)$$

<sup>a</sup> Department of Physics, Indian Institute of Technology Kanpur, 208016, Kanpur, India; E-mail: amitag@iitk.ac.in

<sup>b</sup> NEST-Istituto Nanoscienze and Scuola Normale Superiore, Piazza San Silvestro 12, 56127 Pisa, Italy

<sup>c</sup> Department of Physics, University of Calabria, via ponte Bucci, cubo 31/C 87036, Rende (CS) Italy

<sup>d</sup> Istituto Italiano di Tecnologia-Graphene Labs via Morego 30, 16163 Genova, Italy; E-mail: antonio.politano@iit.it

where  $V_q$  is the Fourier transform of the Coulomb potential,  $n$  is the electron density and  $m^*$  is the effective electron mass. Using the Fourier transform of the long-range Coulomb interaction in two dimensions  $V_q = 2\pi e^2/\kappa q$ , with  $\kappa$  being the static dielectric constant, immediately yields  $\omega_{\text{pl}} \propto \sqrt{q}$ . This square-root dependence of the plasmon dispersion on  $q$  in the long-wavelength limit is a universal feature of two-dimensional electron gases with unscreened Coulomb interaction.

In a quantum mechanical picture, plasmons arise from the poles of the interacting density-density response function, or alternately, as poles of the loss function  $E_{\text{loss}} = \text{Im}[-1/\varepsilon(\omega, q)]$ , where  $\varepsilon(\omega, q)$  is the dynamical dielectric function.<sup>9</sup> The electron energy loss function can be experimentally probed via high-resolution electron energy loss spectroscopy.<sup>11</sup> An effective theoretical approach to calculate the dynamical dielectric function is the random phase approximation (RPA), whereby only Hartree terms (connected single loop diagrams) in the interacting response are retained. Within RPA,  $\varepsilon(\omega, q) \approx 1 - V_q \Pi^0(q, \omega)$ , where  $V_q$  is the Fourier transform of the Coulomb interaction, and  $\Pi^0(q, \omega)$  is the non-interacting density-density response function, which can be calculated using either the effective low-energy, or tight-binding, or ab-initio density functional theory (DFT)-based Hamiltonian.<sup>12</sup> Typically, we have  $V_q \propto 1/q$  for unscreened Coulomb repulsion in 2D, and in the long-wavelength limit we have  $\Pi^0 \propto q^2/\omega^2$ , generally for all materials.<sup>13</sup> Consequently, the zeros of the dynamical  $\varepsilon(\omega, q)$  also lead to  $\omega_{\text{pl}} \propto \sqrt{q}$  in the long-wavelength limit of the quantum mechanical picture as well, consistent with the classical hydrodynamic description for homogeneous response.

While the  $\sqrt{q}$  dependence of the plasmon dispersion in 2D materials is ubiquitous (for unscreened Coulomb repulsion), the dependence of the plasmon energies  $\omega_{\text{pl}}$  on the electron density  $n$  in a 2D semiconductor varies from material to material. For example,  $\omega_{\text{pl}}(q \rightarrow 0) \propto n^{1/2}$  in a parabolically dispersing 2D electron gas (2DEG) with  $E_{\mathbf{k}} = \hbar^2 k^2/(2m)$  and  $\hbar k$  being the crystal momentum, as per Eq. (1). However, for materials with Dirac quasiparticles there is no concept of band mass, and the hydrodynamic description breaks down. An intuitive way to restore the ‘classical’ hydrodynamic description for plasmons of Dirac fermions is to ask what is the analogue of the ‘inertial’ mass in Dirac systems.<sup>13</sup> It turns out that the inertial mass in Dirac materials can be interpreted as the cyclotron mass, which is identical to the band mass for systems with parabolic dispersion. However, in systems with Dirac dispersion, the inertial or the cyclotron mass  $m_c$  has a quantum mechanical origin, and depends on the chemical potential  $\mu$  by the relation,  $m_c = \mu/v_F^2$ , with  $v_F$  denoting the Fermi velocity. As a consequence, the density dependence of long-wavelength plasmons in massless 2D Dirac systems (with  $E_{\mathbf{k}} = \hbar v_F k$ ), such as graphene or borophene, is  $\omega_{\text{pl}}(q \rightarrow 0) \propto n^{1/4}$ . In case of 2D massive Dirac systems with  $E_{\mathbf{k}} = \sqrt{\hbar^2 v_F^2 k^2 + \Delta^2}$ , with  $2\Delta$  denoting the bandgap, this density dependence changes to  $\omega_{\text{pl}}(q \rightarrow 0) \propto n^{1/2}/[n + g\Delta^2/(4\pi\hbar^2 v_F^2)]^{1/4}$ , where  $g$  denotes the spin and valley degeneracy.<sup>14</sup> Thus, in the limit of low densities in massive Dirac systems in 2D (more precisely for  $n \ll \Delta^2/(4\pi\hbar^2 v_F^2)$ ), we have  $\omega_{\text{pl}} \propto n^{1/2}$ , as has been shown for the case of monolayer

MoS<sub>2</sub>, which can be considered as a solid-state example of massive 2D Dirac system.<sup>15</sup>

Additionally, plasmon dispersions of n- and p-doped samples in 2D semiconductors are quite different, due to the marked electron-hole asymmetry, specifically for higher carrier concentrations. Consequently, in 2D semiconductors plasmonic excitations can be tuned by varying the carrier concentration by means of a back gate.

A distinct advantage of plasmons in 2D semiconductors is the relatively large and electrically tunable lifetime of plasmons, which dictates their potential use for technological applications. Note that, within RPA, the plasmon modes are undamped in the regions of the  $(q, \omega)$  space for which  $\text{Im}[\Pi(q, \omega)] = 0$ , and damping processes (the intraband or interband single-particle excitations) are activated wherever  $\text{Im}[\Pi(q, \omega)] \neq 0$ . However, in a realistic scenario, several other decay channels of the plasmonic modes exist, including scattering from impurities, from phonons, multiparticle excitations etc. In 2D semiconductors with a large band gap, the plasmon damping at large momenta is due to the excitation of intraband single-particle excitations, as in MoS<sub>2</sub><sup>15</sup> and black phosphorus.<sup>16</sup> By contrast, in gapless systems, such as graphene, or in small-band-gap materials, like silicene and germanene, plasmons decay in electron-hole pairs via interband transitions.<sup>17</sup>

### 3 Plasmons in 2D semiconductors

Dirac plasmons in graphene behave quite differently with respect to traditional 2D materials, such as III-V semiconductor quantum wells<sup>18</sup>, due to the following reasons: (i) the existence of a pseudospin degree of freedom and (ii) the relativistic nature of Dirac-cone electrons.

As for the case of graphene, transition-metal dichalcogenides (MoS<sub>2</sub>, MoSe<sub>2</sub>, WTe<sub>2</sub> etc.) have a honeycomb lattice without an inversion center.<sup>19</sup> The band structure exhibits a direct gap at the two inequivalent valleys centered at the high-symmetry points  $K$  and  $K' = -K$  in the Brillouin zone.<sup>20</sup> As a consequence of time-reversal symmetry, which maps  $k \rightarrow -k$  and one valley onto the other, electronic states in a specific band at  $K$  and  $K'$  have antiparallel angular momenta. However, the existence of a finite band gap implies that charge carriers in 2D semiconductors cannot behave as massless particles, since they carry a finite effective mass, unlike Dirac fermions in graphene and topological insulators. For this reason, plasmonics with 2D semiconductors share features of both graphene and 2DEG systems.

Plasmonics with 2D semiconductors is strongly influenced by the spin-orbit interaction (SOI), with the subsequent removal of the spin degeneracy. The coexistence of Bychkov-Rashba (BR) and Dresselhaus (D) SOI mechanisms induces highly anisotropic modifications of the static dielectric function<sup>22</sup> and, moreover, the SOI also induces a beating of Friedel oscillations, which can be controlled by external fields. Such a beating phenomenon has been reported for the cases of MoS<sub>2</sub><sup>15</sup> and for buckled honeycomb systems with a remarkable SOI, such as silicene and germanene<sup>21</sup>.

The effective low-energy Hamiltonian of buckled honeycomb structures, such as silicene and germanene, is given by  $H = \hbar v_F (\xi k_x \tau_x + k_y \tau_y) + \Delta_z \tau_z - \xi \Delta_{\text{SO}} \tau_z \sigma_z$ . Here,  $\sigma(\tau)$  denotes the spin

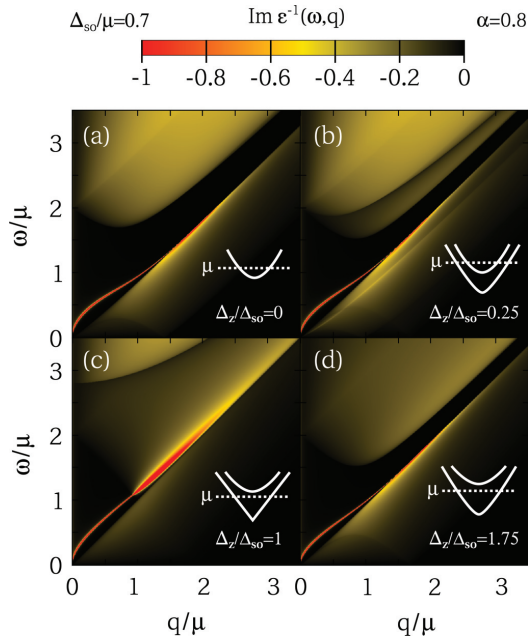


**Fig. 1** The energy loss function for buckled honeycomb lattices, such as silicene or germanene, along with the plasmon dispersion for a fixed  $\Delta_{SO}/\mu = 0.7$  and varying  $\Delta_z$ . Panel (a) is for  $\Delta_z = 0$ , which is the case of a topological insulator, with degenerate spin bands as shown in the sketch of the bands. (b) is for the case of  $\Delta_z/\Delta_{SO} < 1$ , which is the spin-polarized topological-insulator phase as indicated in the sketch of the bands. (c) is for the case of  $\Delta_z/\Delta_{SO} = 1$ , which is a valley spin-polarized semimetal with one set of linear band gapless band, and the other massive Dirac like band as shown in the sketch of the bands. (d) represents the case of  $\Delta_z/\Delta_{SO} > 1$ , which is an ordinary band insulator. The plasmon dispersion is denoted by the red curve in all four panels. Here,  $2\pi e^2/\kappa = 0.8$ . In panels (a), (b) and (c) all the band with the lower (higher) energy correspond to the spin up (down) bands. Adapted with permission from Ref. <sup>21</sup>.

(pseudo-spin) degree of freedom and  $\xi = \pm 1$  for the two inequivalent Dirac points  $K$  and  $K'$ .  $\Delta_{SO}$  represents the gap induced by SOI (1.55 and 24.0 meV for silicene and germanene, respectively<sup>23</sup>).  $\Delta_z = E_z \cdot d$  accounts for the A-B sublattice symmetry breaking, where  $E_z$  is the effective external electric field perpendicular to the sample, including all the screening effects, and  $d$  is the perpendicular distance between the two sublattice planes. The corresponding low-energy dispersion is given by  $E_{\mathbf{k}} = \pm \sqrt{(\hbar v_F |\mathbf{k}|)^2 + \Delta_{s\xi}^2}$ , with the effective gap being  $\Delta_{s\xi} = \Delta_{SO} |s\xi\gamma - 1|$ . Here,  $s = \pm 1$  denotes the spin, and  $\gamma = \Delta_{SO}/\Delta_z$ . Interestingly, tuning the vertical electric field and changing  $\Delta_z$  can change the 2D structure from a band insulator ( $\gamma > 1$ ), to a valley spin-polarized metal ( $\gamma = 1$ ), to a topological insulator ( $\gamma < 1$ ). The most peculiar characteristics of plasmon modes in buckled honeycomb systems is that both their screening processes and the plasmon dispersion can be tuned by changing  $\gamma$ .

The plasmon dispersion in silicene and germanene, when the chemical potential is such that both the conduction bands are occupied [see inset of Fig. 1(b)], is:

$$\omega_{\text{pl}}(q) \approx \sqrt{\frac{\alpha_k v_F \mu q}{\hbar} \left( 2 - \frac{\Delta_+^2 + \Delta_-^2}{\mu^2} \right)}, \quad (2)$$

where  $2\Delta_{\pm} = \Delta_{SO} |\gamma \mp 1|$ , as the spin-dependent energy gaps, and  $\alpha_k$  is the effective fine structure constant. For the case when only one band is occupied, or  $\Delta_- < \mu < \Delta_+$ , the corresponding plasmon dispersion is

$$\omega_{\text{pl}}(q) \approx \sqrt{\frac{\alpha_k v_F \mu q}{\hbar} \left( 1 - \frac{\Delta_-^2}{\mu^2} \right)}. \quad (3)$$

We emphasize again that  $\omega_{\text{pl}}(q) \propto \sqrt{q}$  is a peculiarity of every 2DEG system with long-range Coulomb interactions.<sup>24</sup> By adjusting the electric field, it is possible to tune the plasmon energy, which undergoes a blue-shift as the ratio  $\gamma$  decreases - see Fig. 1. Additionally, the damping processes of plasmon modes in silicene and germanene reflect the change of the topology of the energy bands. For  $\gamma \rightarrow 1$ , the small band gap reduces the lifetime of the plasmon excitation, which could be damped by thermal fluctuation or disorder scattering.<sup>25</sup> For  $\gamma \neq 1$ , the damping of the plasmon mode is suppressed. By evaluating  $\gamma$ , it can be concluded that the lifetime of plasmonic modes in germanene should be rather higher compared to silicene.

Wu et. al.<sup>26</sup> have pointed out the importance of the interplay of SOI and temperature in silicene-based plasmonics. In particular, an additional plasmon branch emerges for  $k_B T \approx E_g$ , where  $k_B$  is the Boltzmann constant and  $E_g$  is the bandgap. Moreover, the lifetime of the plasmon modes is also affected by temperature. Thus, monitoring the plasmon peak, so as to probe abrupt changes in its spectral width and dispersion, could be an useful tool for evaluating temperature-induced changes in SOI. Using the finite temperature polarization function of silicene, germanene and other similar buckled honeycomb structures, it was also shown that the exchange and correlation energies decrease with increasing temperature.<sup>27</sup> Besides the low-energy intraband plasmon, high-energy interband plasmons in such buckled structures have also been studied, both experimentally<sup>28</sup> and theoretically.<sup>29</sup> However, the practical exploitation of high-energy excitations is generally challenging<sup>30</sup>.

Among other 2D semiconductors, the anisotropic lattice of black phosphorus provides novel routes for plasmonics, due to its subsequent band anisotropy. The plasmon disperses differently due to the mass anisotropy, where the smaller mass along the armchair direction leads to higher resonance frequency.<sup>16</sup> For phosphorene, the effective low-energy dispersion in vicinity of the  $\Gamma$  point is given by  $H = (uk_y^2 + \Delta)\tau_x + v_f k_x \tau_y$ , where the subscript  $x/y$  in  $k_{x/y}$  denotes the direction of the armchair/zigzag edge and  $\tau$  denotes the Pauli matrices. The corresponding band dispersion can be further approximated by an anisotropic parabolic dispersion,  $E_{\mathbf{k}} = E_c + \hbar^2 k_x^2 / (2m_x) + \hbar^2 k_y^2 / (2m_y)$ , with  $E_c = \Delta$  being half of the bandgap. The anisotropic band masses are given by<sup>12</sup>  $m_x = \hbar^2 \Delta / v_f^2 \approx 0.2m_e$ , and  $m_y = \hbar^2 / (2u) \approx 1.1m_e$ .

Within the anisotropic mass approximation of the monolayer phosphorene band structure, the long-wavelength plasmon dispersion is given by<sup>12,31</sup>

$$\omega_{\text{pl}}(\mathbf{q}) = \alpha(\mu - E_c)^{1/2} \left[ \cos^2 \theta_q + \frac{m_x}{m_y} \sin^2 \theta_q \right]^{1/2} \sqrt{q}, \quad (4)$$

where  $\theta_q = \tan^{-1}(q_y/q_x)$ ,  $\alpha^2 = 2\pi e^2 g_{2d} / (m_x \kappa)$ , and  $g_{2d} =$

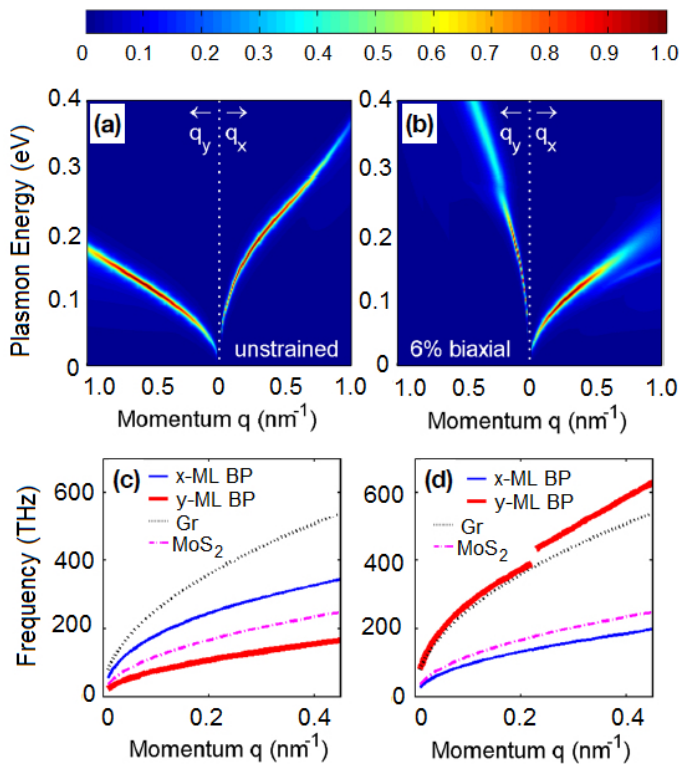


**Fig. 2** (a) The anisotropic plasmon dispersion of monolayer phosphorene. The plasmon mass, being larger in the  $y$  (zigzag) direction of phosphorene, leads to reduced plasmon frequencies as  $\omega_{\text{pl}} \propto m^{-1/2}$ . (b) However, strain inverts the mass anisotropy, and, consequently, biaxially strained phosphorene has larger plasmon frequency along the zigzag edge, as compared to the armchair edge. (c) Comparison of the plasmon dispersion in unstrained graphene (black dotted curve), MoS<sub>2</sub> (magenta dashed-dotted curve) and in phosphorene along the zigzag edge (blue thin curve) and along the armchair edge (red thick curve). (d) Same as in (c) but for 6% biaxially strained phosphorene. The plasmon dispersions of graphene and the MoS<sub>2</sub> are for unstrained systems in both panels (c) and (d). The jump in the plasmon dispersion in panel (d) for phosphorene zigzag edge is due to the presence of a second higher frequency peak in the loss function. Adapted with permission from Ref.<sup>32</sup>.

$\sqrt{m_x m_y} / (\pi \hbar^2)$  is the 2D density of states for an anisotropic parabolic band system. Note that the  $\sqrt{q}$  dependence of the plasmon dispersion in all directions for small wave-vectors is maintained. The anisotropic mass approximation still keeps the  $\omega_{\text{pl}} \propto \mu^{1/2}$  dependence.<sup>16</sup> However, the anisotropy of long-wavelength ( $q \rightarrow 0$ ) plasmon dispersion  $\omega_{\text{pl}}(q\hat{x}) / \omega_{\text{pl}}(q\hat{y}) = \sqrt{m_y/m_x}$  does not depend on the chemical potential of the system. For multilayer phosphorene, the band non-parabolicity caused by interband coupling leads to a plasmon frequency scaling as  $n^\beta$ , where  $n$  is the carrier concentration, and  $\beta < 1/2$ .<sup>16</sup> The non-parabolicity effects are generally more prominent for thicker films of phosphorene.

Another useful feature of plasmonics in phosphorene is the tunability of the band structure via applied strain<sup>33,34</sup> or an out-of-plane static electric field, which can be experimentally implemented via potassium doping.<sup>35</sup> This leads to a significant change in the plasmon dispersion as well<sup>32,36</sup>. For example, strain can invert the anisotropy of the electronic band masses in phospho-

rene<sup>33</sup>, making  $m_x > m_y$ , resulting in higher frequency of the plasmons in along the armchair direction ( $\Gamma - X$ ) compared to the plasmon frequency in the zigzag direction ( $\Gamma - Y$ ), in contrast to the unstrained case [see Fig. 2]. Based on the tunable anisotropic plasmonic response, multilayer phosphorene can be used in anisotropic plasmonic devices.<sup>37</sup>

In addition, black phosphorus has been shown to behave as a 2D hyperbolic material.<sup>38</sup> A hyperbolic material is a highly anisotropic material, for which the components of the permittivity parallel ( $\epsilon_{\parallel}$ ) and perpendicular ( $\epsilon_{\perp}$ ) to the crystal axis have opposite sign.<sup>39</sup> The usually elliptic isofrequency curves of the extraordinary wave become a hyperboloid in black phosphorus. Due to this unique topology, black phosphorus allows the propagation of otherwise evanescent waves.

Black phosphorus also exhibits a surface plasmon polariton (SPP)<sup>40</sup> with extraordinary tunability. More recently, femtosecond photo-switching of interface polaritons in black phosphorus heterostructures has also been demonstrated.<sup>41</sup> The hybrid phonon-plasmon-polariton mode is transient, switchable, exhibits large propagation length, and is likely to be very useful in polariton-based mid-infrared optoelectronic devices.<sup>41</sup>

The plasmonic spectrum of bilayer phosphorene is characterized by two plasmon modes<sup>36</sup>, representing in-phase and out-of-phase oscillations of the carrier density in the two planes, with a dispersion  $\omega_+(q) \propto \sqrt{q}$  and  $\omega_-(q) \propto q$ , respectively.<sup>42</sup> Disorder induces the loss of the decoherence of the  $\omega_-(q)$  mode.

An electric field applied perpendicular to bilayer phosphorene can be used to tune the dispersion of the plasmon modes.<sup>36</sup> For sufficiently large electric field, bilayer phosphorene enters in a topological phase with Dirac-like crossing of bands in one direction and gapped in the other direction. Consequently, the excitation spectrum has different features in this limit, with highly coherent plasmon modes, which are gapped in the armchair direction. Interestingly, the strength of screening of electric fields in black phosphorus<sup>16</sup> ranges between the strong coupling regime characteristic of graphene<sup>43</sup> and the reduced screening properties of transition-metal dichalcogenides.<sup>44</sup>

More recently, several monolayer polymorphs of boron have been experimentally demonstrated.<sup>45,46</sup> In particular, 8-*Pmmn* borophene polymorph has been shown to host massless Dirac fermions with anisotropic and tilted Dirac cone<sup>47,48</sup>. This leads to anisotropic plasmon dispersion, along with anisotropic static screening and Friedel oscillations.<sup>49</sup>

## 4 Potential Applications

The monolayer thickness of 2D semiconductors is an important advantage in many applications, such as field-effect transistors (FETs) for high-performance electronics, sensing applications, and flexible electronics. Nevertheless, in the fields of optoelectronics and photonics the monolayer thickness represents a major challenge concerning the interaction with light, with usually insufficient light emission and absorption. However, several researchers have reported an enhancement of photoluminescence from large-area monolayer MoS<sub>2</sub> using plasmonic noble-metal (Ag or Au) nanostructures.<sup>51-53</sup> As a matter of fact, light can be trapped at MoS<sub>2</sub> with field enhancement near the plasmonic

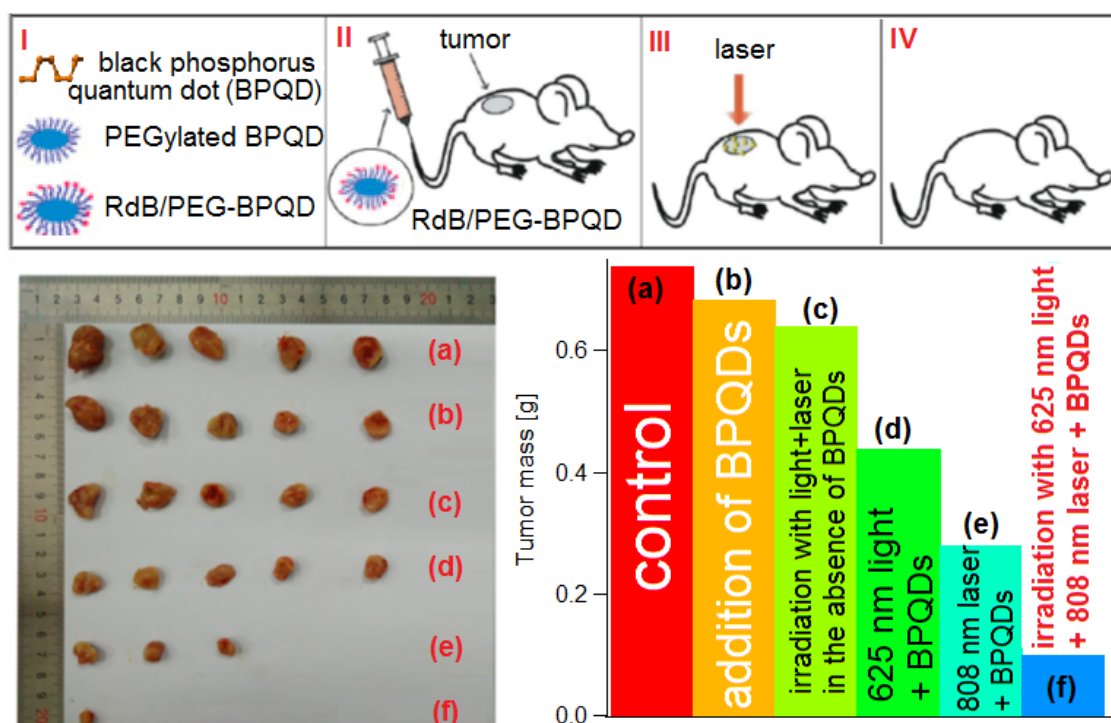


**Fig. 3** In the top part, panel I shows a black phosphorus quantum dot (BPQD), a PEGylated BPQD (where PEG stands for polyethylene glycol), and finally a RdB/PEG BPQD (where RdB stands for rhodamine B). In panel II, the injection of solution containing RdB/PEG BPQDs in a mouse bearing a tumor mass is depicted. Panels III and IV represent the photothermal treatment and the results, i.e. the disappearance of the tumor mass. In the bottom part, (left) photographs of tumors collected from different groups of mice at the end of treatments (16 days) and (right) the average weight of tumors collected from different groups of mice. (group a: control; group b: BPQDs; group c: irradiation with 625 nm light + 808 nm laser; group d: 625 nm light in the presence of BPQDs; group e: 808 nm laser in the presence of BPQDs; group f: 625 nm light + 808 nm laser in the presence of BPQDs). Adapted with permission from Ref. <sup>50</sup>.

nanostructures<sup>54</sup>, with potential exploitation for innovative optoelectronic devices, such as photodetectors and emitters. However, it should be considered that the localized temperature increase at the irradiated nanoparticles, due to photothermal effects, also implies a structural phase transition in MoS<sub>2</sub>.<sup>55</sup>

Studies of photocurrent generation at MoS<sub>2</sub>-metal junctions<sup>56</sup> have indicated that the polarized photocurrent response can be interpreted in terms of the polarized absorption of light by the plasmonic metal electrode, its conversion into hot electron-hole pairs, and subsequent injection into MoS<sub>2</sub>. These fundamental studies shed light on the knowledge of photocurrent generation mechanisms in metal-semiconductor junctions, opening the door for engineering future optoelectronics through SPP in 2D materials.

To extend the operational range of plasmonics with 2D materials, their chemical modification via intercalation is a suitable route. As an example, the electrochemical intercalation on lithium in MoS<sub>2</sub> flakes induces the emergence of plasmon resonances in the visible and near-UV range of the electromagnetic spectrum.<sup>57</sup>

As for conventional plasmonics, biosensing applications have been explored also by using 2D semiconductors.<sup>57,58</sup>

Recent findings for black phosphorus<sup>59,60</sup>, MoS<sub>2</sub><sup>61</sup> and MoSe<sub>2</sub><sup>62</sup> indicate that 2D semiconductors can be suitable also for thermoplasmonics<sup>63-66</sup>, i.e., the thermal heating associated to

optically resonant plasmonic excitations in nanoparticles. Thermoplasmonics relies on the control of nanoscale thermal hotspots by light irradiation.<sup>67</sup> Photothermal effects may be used for enabling plasmon-induced reactions<sup>68-70</sup> or for photothermal treatment of epithelial cancer.<sup>71-74</sup> As sketched in Figure 3, it has been shown that tumor-bearing mice were entirely convalesced after photothermal treatment with nanoparticles of 2D semiconductors.<sup>60</sup> As a matter of fact, quantum dots of 2D semiconductors are characterized by an excellent near-infrared (NIR) photothermal conversion efficiency (28.4 % for black phosphorus<sup>59</sup> and 46.5% for MoSe<sub>2</sub><sup>62</sup>), a large extinction coefficient, as well as good photostability and enhanced stability in physiological medium. In vitro experiments demonstrate that 2D semiconductors have negligible cytotoxicity and can efficiently kill cancer cells under laser irradiation in the visible and NIR range of the electromagnetic spectrum (Figure 3), ensuring the feasibility of thermoplasmonic cancer treatment with 2D semiconductors.

The occurrence of plasmonic modes in the Terahertz (THz) range in the whole class of 2D semiconductors makes them the ideal candidates for plasma-wave THz photodetection. THz represents one of the more exciting technological challenges with extraordinary prospect in the fields of wireless communications, homeland security, night-vision, gas sensing and biomedical applications.<sup>77</sup> The ability to convert light into an electrical signal with high efficiencies and controllable dynamics is a major

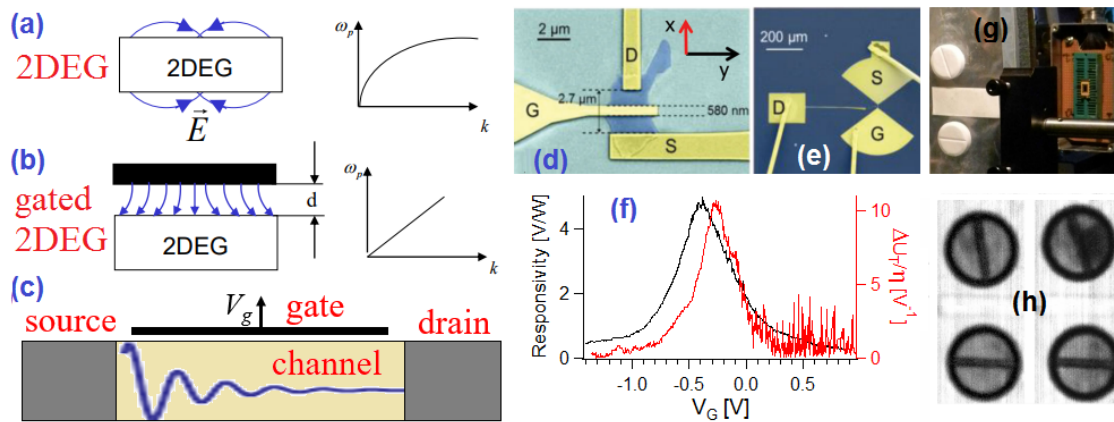


**Fig. 4** Panels (a) and (b) display the dispersion relation of the plasmon frequency in 2DEG and gated 2DEG, respectively. Overdamped propagation of plasma waves, inevitable at room temperature, is sketched in panel (c). In panels (d) and (e) the nanofabrication of THz photodetectors is depicted. Panel (f) shows a comparison between the experimental photoresponse (black curve) and the calculated photoresponse within the framework of the Dyakonov-Shur model<sup>75</sup> (red curve). The two curves qualitatively match, even if the agreement is not perfect, thus implying that the THz photodetection mechanism is not uniquely that one connected with plasma waves. Concerning large-area transmission THz imaging experiments, in panel (g) two tablets before and after injecting a drop of water are displayed. The water content is clearly imaged in the THz transmission image in panel (h). Adapted with permission from Ref.<sup>76</sup>

need in photonics and optoelectronics.<sup>78</sup> The active channel of a FET hosting a 2DEG acts as a cavity for plasma waves, which are described within a hydrodynamic model developed by Dyakonov and Shur.<sup>75</sup> Note that plasma waves propagating in the FET channel cannot be simply identified with the well-known plasmons of a 2DEG<sup>79</sup>, because of the presence of the gate of the FET which induces a linear dispersion relation of the plasma waves (Figure 4, panels a-b). The generated photoresponse  $\Delta u_T$  can be deduced from the transfer characteristics of the FET via the relation<sup>80,81</sup>:

$$\Delta u_T = \frac{1}{\sigma} \cdot \frac{d\sigma}{dV_G} \cdot \left( \frac{R_L}{R_L + \sigma^{-1}} \right) \cdot \eta, \quad (5)$$

where  $\sigma$  is the channel conductivity,  $R_L$  is the finite impedance of the measurement setup including the readout circuitry, and the constant  $\eta$  represents the antenna-dependent coupling efficiency.

In general, the resonant detection, due to the rectification induced by plasma waves, is observed only at cryogenic temperatures. At room temperature, the plasma-wave oscillations are overdamped (Figure 4c), but the rectification mechanism is still efficient and enables a broadband THz detection and imaging<sup>82</sup> (see Figure 4, panels g and h for the case of black-phosphorus THz photodetectors). Recently, Viti et. al.<sup>76,83</sup> used the plasma-wave excitation in the active channel of a phosphorene-based FET (Figure 4, panels c-d) for devising a THz photodetector, whose capabilities are demonstrated by imaging of macroscopic samples, in real time and in a realistic setting (Figure 4, panels g and h). The obtained value of the noise-equivalent power indicates higher performance of 2D semiconductors compared with Dirac materials, such as graphene<sup>80</sup> or topological insulators.<sup>81</sup>

Another promising prospect of plasmonics with 2D semiconductors is related to the fabrication of van der Waals heterostructures<sup>84</sup>, i.e. 2D materials stacked with hexagonal boron nitride. As a matter of fact, recently, graphene stacked with hexagonal boron nitride (h-BN) has been found to act as a hyperbolic metamaterial<sup>85</sup> with unprecedentedly high plasmon lifetime and high

field confinement.<sup>86</sup> Tunability is originated from the hybridization of SPP of the 2D material with hyperbolic phonon polaritons in h-BN<sup>87</sup>, so that the eigenmodes of the van der Waals heterostructure are hyperbolic plasmon-phonon polaritons.

## 5 Conclusions

2D materials beyond graphene offer very interesting plasmonic properties, which are of great interest both from a fundamental as well as technological perspective. A great advantage of 2D materials is the longer lifetime and the tunability of both plasmon dispersion and damping by changing the doping, intercalating chemical species, applying vertical electric fields etc. This facilitates their interaction with light, leading to localization and guiding of light into electrical signals, which can be technologically used for devising plasmonic devices for diverse applications, ranging from nanoelectronics, nanophotonics and nanomedicine.

## References

- 1 F. Bonaccorso, L. Colombo, G. Yu, M. Stoller, V. Tozzini, A. C. Ferrari, R. S. Ruoff and V. Pellegrini, *Science*, 2015, **347**, 1246501.
- 2 A. C. Ferrari, F. Bonaccorso, V. Fal'ko, K. S. Novoselov, S. Roche, P. Boggild, S. Borini, F. H. L. Koppens, V. Palermo, N. Pugno, J. A. Garrido, R. Sordan, A. Bianco, L. Ballerini, M. Prato, E. Lidorikis, J. Kivioja, C. Marinelli, T. Ryhanen, A. Morpurgo, J. N. Coleman, V. Nicolosi, L. Colombo, A. Fert, M. Garcia-Hernandez, A. Bachtold, G. F. Schneider, F. Guinea, C. Dekker, M. Barbone, Z. Sun, C. Galiotis, A. N. Grigorenko, G. Konstantatos, A. Kis, M. Katsnelson, L. Vandersypen, A. Loiseau, V. Morandi, D. Neumaier, E. Treossi, V. Pellegrini, M. Polini, A. Tredicucci, G. M. Williams, B. Hee Hong, J.-H. Ahn, J. Min Kim, H. Zirath, B. J. van Wees, H. van der Zant, L. Occhipinti, A. Di Matteo, I. A. Kinloch, T. Seyller, E. Quesnel, X. Feng, K. Teo, N. Rupasinghe, P. Hakonen, S. R. T. Neil, Q. Tannock, T. Lofwander and J. Kinaret,

- Nanoscale*, 2015, **7**, 4598–4810.
- 3 P. Miro, M. Audiffred and T. Heine, *Chem. Soc. Rev.*, 2014, **43**, 6537–6554.
  - 4 K. Lee, G. Kulkarni and Z. Zhong, *Nanoscale*, 2016, **8**, 7755–7760.
  - 5 Q. Feng, F. Yan, W. Luo and K. Wang, *Nanoscale*, 2016, **8**, 2686–2692.
  - 6 J. Zhu, A. Chroneos and U. Schwingenschlogl, *Nanoscale*, 2016, **8**, 7272–7277.
  - 7 R. K. Ulaganathan, Y.-Y. Lu, C.-J. Kuo, S. R. Tamalampudi, R. Sankar, K. M. Boopathi, A. Anand, K. Yadav, R. J. Mathew, C.-R. Liu, F. C. Chou and Y.-T. Chen, *Nanoscale*, 2016, **8**, 2284–2292.
  - 8 M. Dragoman and D. Dragoman, *Progress in Quantum Electronics*, 2008, **32**, 1–41.
  - 9 G. Giuliani and G. Vignale, *Quantum theory of the electron liquid*, Cambridge university press, 2005.
  - 10 A. N. Grigorenko, M. Polini and K. S. Novoselov, *Nat. Photon*, 2012, **6**, 749–758.
  - 11 M. Rocca, *Surface Science Reports*, 1995, **22**, 1 – 71.
  - 12 B. Ghosh, P. Kumar, A. Thakur, Y. S. Chauhan, S. Bhowmick and A. Agarwal, *Phys. Rev. B*, 2017, **96**, 035422.
  - 13 R. Sachdeva, A. Thakur, G. Vignale and A. Agarwal, *Phys. Rev. B*, 2015, **91**, 205426.
  - 14 A. Thakur, K. Sadhukhan and A. Agarwal, *Phys. Rev. B*, 2018, **97**, 035403.
  - 15 A. Scholz, T. Stauber and J. Schliemann, *Phys. Rev. B*, 2013, **88**, 035135.
  - 16 T. Low, R. Roldán, H. Wang, F. Xia, P. Avouris, L. M. Moreno and F. Guinea, *Phys. Rev. Lett.*, 2014, **113**, 106802.
  - 17 E. H. Hwang and S. Das Sarma, *Phys. Rev. B*, 2007, **75**, 205418.
  - 18 Y. Chen, J. C. Hermanson and G. J. Lapeyre, *Phys. Rev. B*, 1989, **39**, 12682–12687.
  - 19 R. Suzuki, M. Sakano, Y. J. Zhang, R. Akashi, D. Morikawa, A. Harasawa, K. Yaji, K. Kuroda, K. Miyamoto, T. Okuda, K. Ishizaka, R. Arita and Y. Iwasa, *Nat. Nano*, 2014, **9**, 611–617.
  - 20 T. Olsen and I. Souza, *Phys. Rev. B*, 2015, **92**, 125146.
  - 21 C. J. Tabert and E. J. Nicol, *Phys. Rev. B*, 2014, **89**, 195410.
  - 22 S. M. Badalyan, A. Matos-Abiague, G. Vignale and J. Fabian, *Phys. Rev. B*, 2010, **81**, 205314.
  - 23 C.-C. Liu, W. Feng and Y. Yao, *Phys. Rev. Lett.*, 2011, **107**, 076802.
  - 24 F. Stern, *Phys. Rev. Lett.*, 1967, **18**, 546–548.
  - 25 H.-R. Chang, J. Zhou, H. Zhang and Y. Yao, *Phys. Rev. B*, 2014, **89**, 201411.
  - 26 J. Y. Wu, S. C. Chen and M. F. Lin, *New Journal of Physics*, 2014, **16**, 125002.
  - 27 A. Iurov, G. Gumbs and D. Huang, *Journal of Physics: Condensed Matter*, 2017, **29**, 135602.
  - 28 A. Sindona, A. Cupolillo, F. Alessandro, M. Pisarra, D. C. Coello Fiallos, S. M. Osman and L. S. Caputi, *Phys. Rev. B*, 2018, **97**, 041401.
  - 29 C. Vacacela Gomez, M. Pisarra, M. Gravina, P. Riccardi and A. Sindona, *Phys. Rev. B*, 2017, **95**, 085419.
  - 30 B. Fotouhi, V. Ahmadi, M. Abasifard and R. Roohi, *The Journal of Physical Chemistry C*, 2016, **120**, 13693–13700.
  - 31 A. S. Rodin and A. H. Castro Neto, *Phys. Rev. B*, 2015, **91**, 075422.
  - 32 K.-T. Lam and J. Guo, *Journal of Applied Physics*, 2015, **117**, 113105.
  - 33 R. Fei and L. Yang, *Nano Letters*, 2014, **14**, 2884–2889.
  - 34 X. Han, H. M. Stewart, S. A. Shevlin, C. R. A. Catlow and Z. X. Guo, *Nano Letters*, 2014, **14**, 4607–4614.
  - 35 J. Kim, S. S. Baik, S. H. Ryu, Y. Sohn, S. Park, B.-G. Park, J. Denlinger, Y. Yi, H. J. Choi and K. S. Kim, *Science*, 2015, **349**, 723–726.
  - 36 F. Jin, R. Roldán, M. I. Katsnelson and S. Yuan, *Phys. Rev. B*, 2015, **92**, 115440.
  - 37 Z. Liu and K. Aydin, *Nano Letters*, 2016, **16**, 3457–3462.
  - 38 S. A. H. Gangaraj, T. Low, A. Nemilentsau and G. W. Hanson, *IEEE Transactions on Antennas and Propagation*, 2017, **65**, 1174–1186.
  - 39 S. Kalusniak, L. Orphal and S. Sadofev, *Opt. Express*, 2015, **23**, 32555–32560.
  - 40 A. Nemilentsau, T. Low and G. Hanson, *Phys. Rev. Lett.*, 2016, **116**, 066804.
  - 41 M. A. Huber, F. Mooshammer, M. Plankl, L. Viti, F. Sandner, L. Z. Kastner, T. Frank, J. Fabian, M. S. Vitiello, T. L. Cocker and R. Huber, *Nature Nanotechnology*, 2016, **12**, 207.
  - 42 S. Saberi-Pouya, T. Vazifeshenas, M. Saleh, M. Farmanbar and T. Salavati-fard, *ArXiv e-prints*, 2017.
  - 43 S. S. Datta, D. R. Strachan, E. J. Mele and A. T. C. Johnson, *Nano Lett.*, 2009, **9**, 7–11.
  - 44 A. Castellanos-Gomez, E. Cappelluti, R. Roldán, N. Agrait, F. Guinea and G. Rubio-Bollinger, *Advanced Materials*, 2013, **25**, 899–903.
  - 45 B. Feng, J. Zhang, Q. Zhong, W. Li, S. Li, H. Li, P. Cheng, S. Meng, L. Chen and K. Wu, *Nature Chemistry*, 2016, **8**, 563 EP –.
  - 46 A. J. Mannix, X.-F. Zhou, B. Kiraly, J. D. Wood, D. Alducin, B. D. Myers, X. Liu, B. L. Fisher, U. Santiago, J. R. Guest, M. J. Yacaman, A. Ponce, A. R. Oganov, M. C. Hersam and N. P. Guisinger, *Science*, 2015, **350**, 1513–1516.
  - 47 X.-F. Zhou, X. Dong, A. R. Oganov, Q. Zhu, Y. Tian and H.-T. Wang, *Phys. Rev. Lett.*, 2014, **112**, 085502.
  - 48 B. Feng, O. Sugino, R.-Y. Liu, J. Zhang, R. Yukawa, M. Kawamura, T. Iimori, H. Kim, Y. Hasegawa, H. Li, L. Chen, K. Wu, H. Kumigashira, F. Komori, T.-C. Chiang, S. Meng and I. Matsuda, *Phys. Rev. Lett.*, 2017, **118**, 096401.
  - 49 K. Sadhukhan and A. Agarwal, *Phys. Rev. B*, 2017, **96**, 035410.
  - 50 Y. Li, Z. Liu, Y. Hou, G. Yang, X. Fei, H. Zhao, Y. Guo, C. Su, Z. Wang, H. Zhong, Z. Zhuang and Z. Guo, *ACS Applied Materials and Interfaces*, 2017, **9**, 25098–25106.
  - 51 A. Sobhani, A. Lauchner, S. Najmaei, C. Ayala-Orozco, F. Wen,

- J. Lou and N. J. Halas, *Applied Physics Letters*, 2014, **104**, 031112.
- 52 S. Butun, S. Tongay and K. Aydin, *Nano Lett.*, 2015, **15**, 2700–2704.
- 53 S. Najmaei, A. Mlayah, A. Arbouet, C. Girard, J. LPotin and J. Lou, *ACS Nano*, 2014, **8**, 12682–12689.
- 54 J. Miao, W. Hu, Y. Jing, W. Luo, L. Liao, A. Pan, S. Wu, J. Cheng, X. Chen and W. Lu, *Small*, 2015, **11**, 2392–2398.
- 55 Y. Kang, S. Najmaei, Z. Liu, Y. Bao, Y. Wang, X. Zhu, N. J. Halas, P. Nordlander, P. M. Ajayan, J. Lou and Z. Fang, *Advanced Materials*, 2014, **26**, 6467–6471.
- 56 T. Hong, B. Chamlagain, S. Hu, S. M. Weiss, Z. Zhou and Y.-Q. Xu, *ACS Nano*, 2015, **9**, 5357–5363.
- 57 Y. Wang, J. Z. Ou, A. F. Chrimes, B. J. Carey, T. Daeneke, M. M. Y. A. Alsaif, M. Mortazavi, S. Zhuiykov, N. Medhekar, M. Bhaskaran, J. R. Friend, M. S. Strano and K. Kalantar-Zadeh, *Nano Lett.*, 2015, **15**, 883–890.
- 58 A. K. Mishra, S. K. Mishra and R. K. Verma, *The Journal of Physical Chemistry C*, 2016, **120**, 2893–2900.
- 59 Z. Sun, H. Xie, S. Tang, X.-F. Yu, Z. Guo, J. Shao, H. Zhang, H. Huang, H. Wang and P. K. Chu, *Angewandte Chemie*, 2015, **127**, 11688–11692.
- 60 C. Sun, L. Wen, J. Zeng, Y. Wang, Q. Sun, L. Deng, C. Zhao and Z. Li, *Biomaterials*, 2016, **91**, 81 – 89.
- 61 T. Liu, C. Wang, X. Gu, H. Gong, L. Cheng, X. Shi, L. Feng, B. Sun and Z. Liu, *Advanced Materials*, 2014, **26**, 3433–3440.
- 62 L. Yuwen, J. Zhou, Y. Zhang, Q. Zhang, J. Shan, Z. Luo, L. Weng, Z. Teng and L. Wang, *Nanoscale*, 2016, **8**, 2720–2726.
- 63 J. B. Herzog, M. W. Knight and D. Natelson, *Nano Lett.*, 2014, **14**, 499–503.
- 64 M. Essone Mezeme and C. Brosseau, *Phys. Rev. E*, 2013, **87**, 012722.
- 65 R. Rodrguez-Oliveros and J. A. Snchez-Gil, *Opt. Express*, 2012, **20**, 621–626.
- 66 M. Zhu, G. Baffou, N. Meyerbroker and J. Polleux, *ACS Nano*, 2012, **6**, 7227–7233.
- 67 Z. J. Coppens, W. Li, D. G. Walker and J. G. Valentine, *Nano Lett.*, 2013, **13**, 1023–1028.
- 68 S. Mukherjee, F. Libisch, N. Large, O. Neumann, L. V. Brown, J. Cheng, J. B. Lassiter, E. A. Carter, P. Nordlander and N. J. Halas, *Nano Lett.*, 2013, **13**, 240–247.
- 69 C. Gomes Silva, R. Juarez, T. Marino, R. Molinari and H. Garcia, *Journal of the American Chemical Society*, 2011, **133**, 595–602.
- 70 A. Primo, T. Marino, A. Corma, R. Molinari and H. Garcia, *Journal of the American Chemical Society*, 2011, **133**, 6930–6933.
- 71 I. H. El-Sayed, X. Huang and M. A. El-Sayed, *Cancer Letters*, 2006, **239**, 129 – 135.
- 72 C. M. Hessel, V. P. Pattani, M. Rasch, M. G. Panthani, B. Koo, J. W. Tunnell and B. A. Korgel, *Nano Lett.*, 2011, **11**, 2560–2566.
- 73 B. Khlebtsov, V. Zharov, A. Melnikov, V. Tuchin and N. Khlebtsov, *Nanotechnology*, 2006, **17**, 5167.
- 74 J. Z. Zhang, *The Journal of Physical Chemistry Letters*, 2010, **1**, 686–695.
- 75 M. Dyakonov and M. Shur, *IEEE Transactions on Electron Devices*, 1996, **43**, 380–387.
- 76 L. Viti, J. Hu, D. Coquillat, A. Politano, W. Knap and M. S. Vitiello, *Scientific Reports*, 2016, **6**, 20474.
- 77 S. S. Dhillon, M. S. Vitiello, E. H. Linfield, A. G. Davies, M. C. Hoffmann, J. Booske, C. Paoloni, M. Gensch, P. Weightman, G. P. Williams, E. Castro-Camus, D. R. S. Cumming, F. Simoens, I. Escorcia-Carranza, J. Grant, S. Lucyszyn, M. Kuwata-Gonokami, K. Konishi, M. Koch, C. A. Schmuttenmaer, T. L. Cocker, R. Huber, A. G. Markelz, Z. D. Taylor, V. P. Wallace, J. A. Zeitler, J. Sibik, T. M. Korter, B. Ellison, S. Rea, P. Goldsmith, K. B. Cooper, R. Appleby, D. Pardo, P. G. Huggard, V. Krozer, H. Shams, M. Fice, C. Renaud, A. Seeds, A. Stohr, M. Naftaly, N. Ridler, R. Clarke, J. E. Cunningham and M. B. Johnston, *Journal of Physics D: Applied Physics*, 2017, **50**, 043001.
- 78 F. H. L. Koppens, T. Mueller, P. Avouris, A. C. Ferrari, M. S. Vitiello and M. Polini, *Nat. Nano*, 2014, **9**, 780–793.
- 79 A. Tomadin and M. Polini, *Phys. Rev. B*, 2013, **88**, 205426.
- 80 L. Vicarelli, M. S. Vitiello, D. Coquillat, A. Lombardo, A. C. Ferrari, W. Knap, M. Polini, V. Pellegrini and A. Tredicucci, *Nat. Mater*, 2012, **11**, 865–871.
- 81 L. Viti, D. Coquillat, A. Politano, K. A. Kokh, Z. S. Aliev, M. B. Babanly, O. E. Tereshchenko, W. Knap, E. V. Chulkov and M. S. Vitiello, *Nano Lett.*, 2016, **16**, 80–87.
- 82 W. Knap, M. Dyakonov, D. Coquillat, F. Teppe, N. Dyakonova, J. Łusakowski, K. Karpierz, M. Sakowicz, G. Valusis, D. Seluta, I. Kasalynas, A. El Fatimy, Y. M. Meziani and T. Otsuji, *Journal of Infrared, Millimeter, and Terahertz Waves*, 2009, **30**, 1319–1337.
- 83 L. Viti, J. Hu, D. Coquillat, W. Knap, A. Tredicucci, A. Politano and M. S. Vitiello, *Advanced Materials*, 2015, **27**, 5567–5572.
- 84 A. K. Geim and I. V. Grigorieva, *Nature*, 2013, **499**, 419–425.
- 85 S. Dai, Q. Ma, M. K. Liu, T. Andersen, Z. Fei, M. D. Goldflam, M. Wagner, K. Watanabe, T. Taniguchi, M. Thiemens, F. Keilmann, G. C. A. M. Janssen, S.-E. Zhu, P. Jarillo-Herrero, M. M. Fogler and D. N. Basov, *Nat. Nano*, 2015, **10**, 682–686.
- 86 A. Woessner, M. B. Lundberg, Y. Gao, A. Principi, P. Alonso-Gonzalez, M. Carrega, K. Watanabe, T. Taniguchi, G. Vignale, M. Polini, J. Hone, R. Hillenbrand and F. H. L. Koppens, *Nat. Mater*, 2015, **14**, 421–425.
- 87 C. R. Dean, A. F. Young, I. Meric, C. Lee, L. Wang, S. Sorgenfrei, K. Watanabe, T. Taniguchi, P. Kim, L. K. Shepard and J. Hone, *Nat. Nano*, 2010, **5**, 722–726.